Article:
Wu, Z-F., Xu, H-P., Li, J-W. et al. (1 more author) (2015) Passive Interfering Method for InSAR Based on Circularly Moving Strong Scatterers. IEEE Transactions on Aerospace and Electronic Systems, 51 (3). pp. 1877-1890. ISSN 0018-9251

https://doi.org/10.1109/TAES.2015.130437

A Passive Interfering Method for InSAR Based on Circularly Moving Strong Scatterers

Zhe-feng Wu, Hua-ping Xu, Jing-wen Li, Wei Liu

School of Electronic and Information Engineering, Beihang University, Beijing, 100191, China

e-mail: wuzheming001@126.com

***Abstract*—A novel jamming method based on circularly moving strong scatterers is proposed. The jamming signal model is firstly presented and the corresponding imaging results are derived through a Range-Doppler algorithm. Detailed analysis shows that the proposed method can decrease the correlation, produce interferometric phase bias, result in failure of phase unwrapping and reduce the accuracy of digital elevation model (DEM). Simulation results are provided to verify the effectiveness of the proposed method.**

***Index Terms*—jamming, interferometry, synthetic aperture radar (SAR), strong scatterer, passive interference.**

I. INTRODUCTION

Synthetic Aperture Radar, as an all-weather all-time remote sensing technique, has been widely used in both military and civilian applications, such as monitoring, geological investigation and ground moving target recognition [1]-[3]. InSAR, a further development of the traditional SAR technology, employs two or more SAR antennas to obtain the elevation information of the ground surface by measuring the phase difference between the dual images [2]. For the dual-pass InSAR, the master

antenna and the slave antenna transmit and receive SAR signals by themselves. When InSAR works in the single-pass mode, the master antenna serves as a transmitter and both antennas record the echo signals simultaneously [2], [3].

In the past, several working InSAR systems have been deployed. The satellite TanDEM-X, launched in 2010, can achieve a DEM precision as small as 2 m [4]. The Shuttle Radar Topography Mission (SRTM), with two antennas using single-pass InSAR and operating at a wavelength of 5.6 cm, produced the most accurate near-global DEM covering most land and adjacent near-shore ocean areas between latitudes 56° south and 60° north [5]. RADARSAT-1 and RADARSAT-2, the Canadian SAR remote sensing satellites, are still fully operational and continue to provide InSAR data to worldwide users [6]. All these systems have high measuring accuracy and can detect a variety of important targets effectively for different purposes.

Meanwhile, in order to protect important facilities against military reconnaissance, the development of effective jamming methods for InSAR has become more and more important. On the other hand, research on jamming methods can help identify the weakness of current InSAR systems, so that more effective and robust systems with further improved performance can be developed in the future to work in complicated real-world scenarios.

With the need and rapid development of electronic countermeasures (ECM), a large amount of work has been focused on the jamming of airborne or spaceborne SAR systems. In [7], [8], different types of ECM jamming signals were introduced and they are now used widely. Digital Radio Frequency Memory (DRFM), a low-cost and yet very effective ECM jamming method, was introduced in [9], by retransmitting a replica of the received signals. A detailed study for large scene deceptive jamming was provided in [10], based on which a fast algorithm was then proposed. Although these traditional barrage

jamming [7], DRFM and deceptive interference can jam the amplitude of the SAR image to different degrees, the phase part is cancelled through interferometry. As a result, their interfering effects on interferometry are limited. Cross-eye jamming, with two jammer antennas simultaneously transmitting the interference, generates angle jamming for the threat radar, which is usually applied to against a monopulse radar [11]-[14]. However, the idea of multi-antenna jamming provides a possible method for jamming InSAR. In the cross-eye jamming, the interference transmitted by the two antennas of jammer will produce the phase noise in the resultant interferogram. Since the resultant phase noise is simultaneously affected by both the magnitude and the phase of the intererence, the whole situation will be more complicated. Therefore, an in-depth study of the effect of multi-antenna interference is needed for its application in InSAR jamming.

In this paper, we propose a novel method based on circularly moving strong scatterers, suitable for jamming both airborne and spaceborne InSAR systems. Different from conventional SAR jamming methods, the new method is aimed to change the interferometric phase information of the real scene to significantly reduce the accuracy of DEM or result in loss of some terrain features.

Corner reflectors are originally used for external calibration of SAR systems [15]. Circular motion of the corner reflector with a certain angular speed in the horizontal plane will result in varying time delays and lead to changes in Doppler frequency [16]-[18]. The difference in Doppler frequency has a defocusing effect on the jamming signal along the azimuth direction, which can produce phase perturbations different from each other at both antennas. The resultant phase noise distributed along the azimuth direction will cause significant errors to the interferometric phase of the real scene. As a result, compared to the traditional SAR jamming method, the new method can reduce the accuracy of elevation estimation of the InSAR system significantly.

There are two major advantages with the proposed method. Firstly, as a passive interfering technique, it is energy saving by reflecting the transmitted signal of the threat radar effectively. Although the reflected energy is limited, the jamming effect can be improved as the density and the coverage of strong scatterers increase. Secondly, since signal detection and analysis equipment is not used, the cost is much lower than traditional electronic jamming systems. Moreover, study of target micromotion characteristics has attracted more and more interest recently and the research result for circularly moving strong scatterers obtained here can be applied to study the influence of target micromotion on SAR and InSAR in the future. The remainder of this paper is organized as follows. Signal models and the imaging outputs at the two antennas due to circularly moving strong scatterers are given in Section II. In Section III, the interferometric phase model for the proposed method is derived and the effect of jamming on correlation and elevation estimation accuracy is analyzed. Simulation results are provided in Section IV and conclusions are drawn in Section V.

II. Circularly Moving Strong Scatterer Jamming for SAR Imaging

For circularly moving strong scatterer jamming, we first establish the jamming geometry and, then, the imaging results in two antennas models are derived. Generally, many targets belong to strong scatterers. Without loss of generality, we use corner reflectors for analysis below.

A. Principle of Circularly Moving Strong Scatterer Jamming

The ECM scenario is shown in Fig. 1(a). Points A_1 and A_2 represent the master antenna and the slave antenna, respectively. The SAR platform flies along the x-axis in a fixed altitude and images an area on the ground plane. θ denotes the look angle, H is the flight altitude of the master antenna,

and XOY (ground plane) is the target focus plane. In Fig. 1(b), θ_0 is the initial angle value. The corner reflector moves in a circular path around the center (x_0, y_0, z_0) on the horizontal plane with a radius r and an angular speed ω, as shown in Fig. 1(b).

As the reflector moves around a fixed datum, both antennas receive echoes from the real scene and the reflector simultaneously. The circularly moving corner reflector echoes will further affect the imaging results and interferometric processing of InSAR. In what follows, we will give an analysis of both the signal model and the imaging output for the circularly moving corner reflector.

B. Echo Signal Model for Circularly Moving Strong Scatterer Jamming

In practice, to achieve a high range resolution, the sensor usually transmits LFM signals. Assume that the signal transmitted by the master antenna A_1 is

$$S_m(t_r) = \text{rect}\left[\frac{t_r}{T_P}\right]\exp\left\{j2\pi\left[f_c t_r + \frac{1}{2}K_r t_r^{\,2}\right]\right\} \tag{1}$$

where t_r is the fast (range) time, T_P is the pulse duration, f_c and K_r denote the carrier frequency and the chirp rate, respectively, and $\text{rect}[\square]$ is the rectangular window function [1]-[3].

The corner reflector reflects echo signals as the SAR platform passes by. Assume that the system works in the side-looking mode. After down-converting, the pulse backscattered from the corner reflector for jamming the master image can be expressed as

$$J_m(t_r, t_a) = \text{rect}\left[\frac{t_r - 2R_{mj}(t_a)/c}{T_P}\right]\text{rect}\left[\frac{t_a}{T_L}\right]\exp\left\{j\pi\left[K_r\left(t_r - \frac{2R_{mj}(t_a)}{c}\right)^2\right]\right\}\exp\left\{-j\frac{4\pi R_{mj}(t_a)}{\lambda}\right\} \tag{2}$$

where c is the speed of light, T_L denotes the synthetic aperture time, λ is the wavelength, and $R_{mj}(t_a)$ is the instantaneous slant range between the phase center of InSAR master antenna and the position of corner reflector with respect to slow time t_a. The instantaneous position of the corner

reflector can be defined as ($x_c + r\cos(\omega t_a + \theta_0)$, $y_c + r\sin(\omega t_a + \theta_0)$, z_c). Using Taylor series expansion, $R_{mj}(t_a)$ is approximated as

$$\begin{aligned} R_{mj}(t_a) &= \sqrt{\left[x_0 + r\cos\left(\omega t_a + \theta_0\right) - vt_a\right]^2 + \left[y_0 + r\sin\left(\omega t_a + \theta_0\right)\right]^2 + \left(z_0 - H\right)^2} \\ &\approx R_M + \frac{r^2 + \left(x_0 - vt_a\right)^2 + 2r\sqrt{{y_0}^2 + \left(x_0 - vt_a\right)^2}\sin\left[\omega t_a + \theta_0 + \theta'_m(t_a)\right]}{2R_M} \end{aligned} \tag{3}$$

where v is the velocity of the SAR platform, R_M is the minimum slant range between the master antenna and the rotation center of circularly moving corner reflector, and $\theta'(t_a)$ is given by

$$\theta'_m(t_a) = \arctan\left(\frac{x_0 - vt_a}{y_0}\right) \tag{4}$$

Similarly, the interference received by the slave antenna can be expressed as

$$J_s(t_r, t_a) = \mathrm{rect}\left[\frac{t_r - 2R_{sj}(t_a)/c}{T_P}\right]\mathrm{rect}\left[\frac{t_a}{T_L}\right]\exp\left\{j\pi\left[K_r\left(t_r - \frac{2R_{sj}(t_a)}{c}\right)^2\right]\right\}\exp\left\{-j\frac{4\pi R_{sj}(t_a)}{\lambda}\right\} \tag{5}$$

where $R_{sj}(t_a)$ is the instantaneous slant range between the slave antenna and the corner reflector, given by

$$R_{sj}(t_a) = \sqrt{\left[x_0 + r\cos\left(\omega t_a + \theta_0\right) - vt_a\right]^2 + \left[y_0 + r\sin\left(\omega t_a + \theta_0\right) - B\cos(\alpha)\right]^2 + \left[z_0 - H - B\sin(\alpha)\right]^2} \tag{6}$$

where B is the length of the baseline, α denotes the inclination of the baseline.

C. SAR Imaging Model for Jamming

We now derive the imaging signal model due to jamming in the dual-pass mode. There are different imaging algorithms available and they all achieve the same imaging result. Without loss of generality and for simplicity, we adopt the Range-Doppler algorithm here [19].

First, range matched filtering is performed to (2) using the filter

$$H_{r\_ref}(t_r) = rect\left[\frac{t_r}{T_P}\right]\exp\left\{-j\pi K_r {t_r}^2\right\} \tag{7}$$

The range-compressed signal of the interference in the master image is given by

$$\begin{aligned} J_{m\_rc}(t_r,t_a) &= \int J_m(\tau,t_a)H_{r\_ref}(t_r-\tau)d\tau \\ &= T_P rect\left[\frac{t_a}{T_L}\right]\text{sinc}\left\{B_r\left[t_r-\frac{2R_{mj}(t_a)}{c}\right]\right\}\exp\left\{-j\frac{4\pi R_{mj}(t_a)}{\lambda}\right\} \end{aligned} \tag{8}$$

where B_r represents the range bandwidth of the echo. For different rotational angular velocity, the interference after Range Compression (RC) and before Range Cell Migration Correction (RCMC) is given in Fig. 2. Since $R_M >> r$, the terms related to r in (3) are ignored. The signal formulation after RCMC is given by

$$J_{m\_rc}(t_r,t_a) \approx T_P \cdot \text{rect}\left[\frac{t_a}{T_L}\right]\text{sinc}\left\{B_r\left[t_r-\frac{2R_M}{c}\right]\right\}\exp\left\{-j\frac{4\pi R_{mj}(t_a)}{\lambda}\right\} \tag{9}$$

Substituting (3) into (9), we have

$$\begin{aligned} J_{m\_rc}(t_r,t_a) = T_P \cdot \text{rect}\left[\frac{t_a}{T_L}\right]\text{sinc}\left\{B_r\left[t_r-\frac{2R_M}{c}\right]\right\}\exp\left\{-j\frac{4\pi R_M}{\lambda}\right\}\exp\left\{-j\frac{2\pi}{\lambda}\left[\frac{r^2+(vt_a-x_0)^2}{R_M}\right]\right\} \\ \cdot\exp\left\{j\frac{4\pi}{\lambda}r_0(t_a)\sin\left[\omega t_a+\theta_0+\theta'_m(t_a)\right]\right\} \end{aligned} \tag{10}$$

where $r_0(t_a)$ is defined as (As shown in Appendix A)

$$r_0(t_a) = r\sqrt{y_0^2+(vt_a-x_0)^2}\,/\,R_M \approx r\sqrt{y_0^2+(vt_a-x_0)^2}\,/\,R_S \tag{11}$$

For azimuth compression, Bessel function of the first kind is used [20], which is given by

$$\exp\{jx\sin(\vartheta)\} = \sum_{n=-\infty}^{+\infty} J_n(x)\exp\{jn\vartheta\} \tag{12}$$

where $J_n(\square)$ represents the nth Bessel function of the first kind. Substituting (12) into (10), $J_{m\_rc}(t_r,t_a)$ changes to

$$\begin{aligned} J_{m\_rc}(t_r,t_a) = T_P \cdot \text{rect}\left[\frac{t_a}{T_L}\right]\text{sinc}\left\{B_r\left[t_r-\frac{2R_M}{c}\right]\right\}\cdot\exp\left\{-j\frac{4\pi R_M}{\lambda}\right\}\exp\left\{-j\frac{2\pi}{\lambda}\left[\frac{r^2+(vt_a-x_0)^2}{R_M}\right]\right\} \\ \cdot\sum_{n=-\infty}^{+\infty} J_n\left[\frac{4\pi}{\lambda}r_0(t_a)\right]\exp\left\{jn\left[\omega t_a+\theta_0+\theta'_m(t_a)\right]\right\} \end{aligned} \tag{13}$$

Let K_{a1} be the Doppler chirp rate of the master image [18], [20]. Then azimuth matched filtering is performed to (13) using the filter

$$H_{a\_ref}(t_a) = \text{rect}\left[\frac{t_a}{T_L}\right]\exp\left\{j\pi K_{a1}{t_a}^2\right\} \tag{14}$$

The imaging output of the interference displayed in the master image is expressed as

$$\begin{aligned} J_{m\_out}(t_r,t_a) \approx T_P T_L \cdot \text{sinc}\left\{B_r\left[t_r - \frac{2R_M}{c}\right]\right\}\exp\left\{-j\frac{4\pi}{\lambda}\left[R_M + \frac{r^2}{2R_M}\right]\right\} \\ \cdot \sum_{n=-\infty}^{+\infty} J_n\left[\frac{4\pi}{\lambda}r_0(t_a)\right]\text{sinc}\left\{B_a\left(t_a - \frac{n\omega}{2\pi K_{a1}} - \frac{x_0}{v}\right)\right\}\exp\left\{jn\left[\theta_0 + \theta'_m(t_a)\right]\right\} \end{aligned} \tag{15}$$

Similar to (15), the imaging output of the slave antenna is given by

$$\begin{aligned} J_{s\_out}(t_r,t_a) \approx T_P T_L \cdot \text{sinc}\left\{B_r\left[t_r - \frac{2R_S}{c}\right]\right\}\exp\left\{-j\frac{4\pi}{\lambda}\left[R_S + \frac{r^2}{2R_S}\right]\right\} \\ \cdot \sum_{n=-\infty}^{+\infty} J_n\left[\frac{4\pi}{\lambda}r_0(t_a)\right]\text{sinc}\left\{B_a\left(t_a - \frac{n\omega}{2\pi K_{a2}} - \frac{x_0}{v}\right)\right\}\exp\left\{jn\left[\theta_0 + \theta'_s(t_a)\right]\right\} \end{aligned} \tag{16}$$

where R_S is the minimum slant range between the phase center of the InSAR slave antenna and the circularly moving corner reflector, and

$$\theta'_s(t_a) = \arctan\left[\frac{x_0 - vt_a}{y_0 - B\cos(\alpha)}\right] \tag{17}$$

Clearly, according to Carson's rule [20], the exponent terms of (12) will introduce multiple symmetric Doppler shifts and paired echoes of the original signal. The value of the nth paired echoes is determined by $J_n\left[4\pi r_0(t_a)/\lambda\right]$. In Fig. 3, the imaging output for the corner reflector interference is shown, with parameters of the reflector listed in Table I and parameters of the InSAR system in Table II.

III. Circularly Moving Strong Scatterer Jamming for InSAR

In section II, it is shown that the paired echoes, due to circularly moving strong scatterer jamming,

are distributed along the azimuth direction in two SLC images. On the one hand, the jamming will decrease correlation of the two SLC images and reduce the estimation accuracy of the interferometric phase, which will lead to discontinuities of the unwrapped phase. On the other hand, the phases of paired echoes in the same location of two SLC images are different from each other. The phase bias, defined as the bias of interferometric phase due to circularly moving strong scatterer jamming, will result in more errors to the real phase. Therefore, the circularly moving strong scatterer can increase phase errors through two different ways: the correlation of two SLC images and the phase bias of jamming. In this section, the phase bias caused by the paired echoes will be derived, with an analysis of the jamming effect on correlation considered subsequently. Furthermore, the evaluation of DEM errors based on phase noise of the interference is provided.

A. Interferomtric Phase Analysis for Jamming

Interferometric phase, as the basis of elevation measurement, can directly affect the accuracy of DEM [21]. If the two SLC images are accurately co-registered, the phase difference due to jamming can be derived through conjugate multiplication of the two co-registered SAR images.

In the dual-pass mode, the discrepancy between $t_r - 2R_M / c$ and $t_r - 2R_S / c$ in both (15) and (16) will cause an envelope shift between $J_{m\_out}(t_r, t_a)$ and $J_{s\_out}(t_r, t_a)$. This difference can be compensated by high precision image co-registration processing. By assuming that the slave image (16) is adjusted in the light of the master image, $J_{s\_out}(t_r, t_a)$ is rearranged as

$$\begin{aligned} J_{s\_out}(t_r, t_a) \approx T_P T_L \cdot \mathrm{sinc}\left\{ B_r \left[t_r - \frac{2R_M}{c} \right] \right\} \exp\left\{ -j \frac{4\pi}{\lambda} \left[R_S + \frac{r^2}{2R_S} \right] \right\} \\ \cdot \sum_{n=-\infty}^{+\infty} J_n \left[\frac{4\pi}{\lambda} r_0(t_a) \right] \mathrm{sinc}\left\{ B_a \left(t_a - \frac{n\omega}{2\pi K_{a2}} - \frac{x_0}{v} \right) \right\} \exp\left\{ jn\left[\theta_0 + \theta_s'(t_a) \right] \right\} \end{aligned} \tag{18}$$

Ignoring the influence of different Doppler chirp rates on the location of point series and comparing the phases in both (15) and (18), we can derive the phase difference of the paired echoes as

$$\varphi_{IF} = -\frac{4\pi(R_M - R_S)}{\lambda} - \frac{2\pi r^2}{\lambda}\left(\frac{1}{R_M} - \frac{1}{R_S}\right) + \sum_{n=-\infty}^{+\infty} n\left[\theta'_m(t_a) - \theta'_s(t_a)\right] \tag{19}$$

where the first term represents the position of the rotation center, and the remaining terms constitute the phase interference.

Phase noise caused by the paired echoes is generated in the imaging process and the jamming result can be considered as a series of interference signals with phase noises (as shown in Fig. 4.). The interferences will not only affect the two SLC images, but also jam the interferometric phase or even lead to failure of the phase unwrapping process.

B. Jamming Effect on Correlation

Correlation, a measure of similarity between two SLC images, is determined by properties of received signals and several system parameters [22]. In what follows, we will give an analysis of the jamming effect on correlation.

The correlation γ of two SLC images S_1 and S_2 is defined as

$$\gamma = \frac{\left|\left\langle S_1 \square S_2^* \right\rangle\right|}{\sqrt{\left\langle S_1 \square S_1^* \right\rangle \left\langle S_2 \square S_2^* \right\rangle}} \tag{20}$$

where $(\square)^*$ denotes complex conjugate, and $\langle \square \rangle$ represents the ensemble average [22]. The average power of the cross multiplication of the corresponding pixel pairs of the two co-registered SAR images is given by

$$\left\langle S_1 \square S_2^* \right\rangle = \left\langle \left(S_{real\_m} + J_{m\_out}\right)\left(S_{real\_s} + J_{s\_out}\right)^* \right\rangle = \left\langle S_{real\_m} S^*_{real\_s} \right\rangle + \left\langle J_{m\_out} J^*_{s\_out} \right\rangle \tag{21}$$

where S_{real_m} and S_{real_s} represent the corresponding pixels in two SAR images without jamming,

respectively. Then, the individual signal powers of the jammed pixels are given by

$$\left\langle S_1 \square S_1^* \right\rangle = \left\langle S_{real\_m} S^*_{real\_m} \right\rangle + \left\langle J_{m\_out} J^*_{m\_out} \right\rangle \tag{22}$$

$$\left\langle S_2 \square S_2^* \right\rangle = \left\langle S_{real\_s} S^*_{real\_s} \right\rangle + \left\langle J_{s\_out} J^*_{s\_out} \right\rangle \tag{23}$$

Substituting (21), (22) and (23) into (20), we obtain the correlation of the jammed pixels as

$$\gamma = \frac{\left| \left\langle S_{real\_m} S^*_{real\_s} \right\rangle + \left\langle J_{m\_out} J^*_{s\_out} \right\rangle \right|}{\sqrt{\left(\left\langle S_{real\_m} S^*_{real\_m} \right\rangle + \left\langle J_{m\_out} J^*_{m\_out} \right\rangle \right) \left(\left\langle S_{real\_s} S^*_{real\_s} \right\rangle + \left\langle J_{s\_out} J^*_{s\_out} \right\rangle \right)}} \tag{24}$$

To simplify the analysis, we have the following considerations

$$\begin{cases} \left\langle S_{real\_m} S^*_{real\_m} \right\rangle = \left\langle S_{real\_s} S^*_{real\_s} \right\rangle = A^2 \\ \left\langle J_{m\_out} J^*_{m\_out} \right\rangle = \left\langle J_{s\_out} J^*_{s\_out} \right\rangle = {A_J}^2 \\ \left\langle S_{real\_m} S^*_{real\_s} \right\rangle = A^2 \gamma_0 \cdot \exp\{ j\phi_0 \} \\ \left| \left\langle J_{m\_out} J^*_{s\_out} \right\rangle \right| = {A_J}^2 \gamma_J \exp\{ j\phi_J \} \end{cases} \tag{25}$$

where γ_0 and γ_J represent the correlations of the original pixel pairs and the jamming part, respectively, and ϕ_0 and ϕ_J denote the corresponding phases. Substituting (25) into (24), the correlation of the jammed pixels becomes

$$\gamma = \frac{\left| A^2 \gamma_0 \cdot \exp\{ j\phi_0 \} + {A_J}^2 \gamma_J \exp\{ j\phi_J \} \right|}{A^2 + {A_J}^2} \tag{26}$$

Clearly, the ideal correlation without interference is given by γ_0 and it satisfies $\gamma_0 < 1$. For $\gamma_J < \gamma_0$ in equation (26), we obtain $\gamma < \gamma_0$ (As shown in Appendix B). Considering the phase of the jamming part is different from that of SAR images, γ in equation (26) will be smaller. In effect, the input jamming to signal ratio (JSR) in a real scenario is much larger than 0 dB, and we have $\gamma_J \approx \gamma_0$. Thus, the correlation of the jammed pixel pairs is mainly determined by correlation of the jamming parts, and the effect of jamming on the correlation will be more prominent, leading to even smaller values.

The correlation map, as the map of correlation coefficients extracted from the InSAR data, is the best

indicator of the quality of the resultant phase data. According to the parameters listed in Tables I and II, a ground area is established in our simulation. As shown in Fig. 5(a), the correlation coefficients of the ground image without jamming are greater than 0.9. For the case with jamming, a single circularly moving corner reflector is placed at the center of the scene, and the input JSR is 35 dB. As shown in Fig. 5(b), the correlation values within the jammed area is far less than those without jamming. In this case, a failure of the unwrapping process is inevitable, and we will not be able to obtain the correct elevation information of the terrain.

C. Jamming Effect on Elevation Estimation

DEM, as a digital model or 3D representation of a terrain's surface, is created by phase unwrapping and inversion [23]. The accuracy of DEM and DEM-derived products mainly depends on phase errors caused by phase interferences. The mathematical formulation for DEM errors is derived in this subsection by exploiting the general relationship between DEM and the interferometric phase.

After topographic phase unwrapping, the sensitivity of DEM deflection (Δh) on topographic phase ($\Delta\phi$) can be described as:

$$\frac{\Delta\phi}{\Delta h} = -\frac{4\pi B_{\perp}}{\lambda R_0 \sin\theta} \tag{27}$$

where $B_{\perp}$ denotes the baseline component perpendicular to the view line, R_0 is the range between the target and the SAR master antenna , and θ represents the viewing angle of the target [23].

For the height of the topography is approximated by DEM, the elevation error for each pixel caused by phase jamming is expressed as

$$h_{\varepsilon} = -\frac{\lambda R_0 \sin\theta}{4\pi B_{\perp}}\phi_{\varepsilon} \tag{28}$$

According to the position of jamming, the real phase of the jammed pixel is given by

$$\varphi_{real} = -\frac{4\pi\left(R_M - R_S\right)}{\lambda} \tag{29}$$

Therefore, the phase error for the jammed pixel is expressed as

$$\phi_\varepsilon = \varphi_{IF} - \varphi_{real} = -\frac{2\pi r^2}{\lambda}\left(\frac{1}{R_M} - \frac{1}{R_S}\right) + \sum_{n=-\infty}^{+\infty} n\left[\theta'_m(t_a) - \theta'_s(t_a)\right] \tag{30}$$

As the order of the Bessel function, n also represents a different azimuth position, and it is related to the slow time t_a by

$$n = \frac{2\pi K_{a1} t_a}{\omega} \tag{31}$$

Substituting (30) and (31) into (28), we have

$$h_\varepsilon = \frac{\lambda R_M \sin\theta}{4\pi B\cos(\theta-\alpha)}\left\{\frac{2\pi r^2}{\lambda}\left(\frac{1}{R_M} - \frac{1}{R_S}\right) - \frac{2\pi K_{a1} t_a}{\omega}\left[\theta'_m(t_a) - \theta'_s(t_a)\right]\right\} \tag{32}$$

where

$$R_0 = R_M \tag{32a}$$

$$B_\perp = B\cos(\theta-\alpha) \tag{32b}$$

From (32), we see that the DEM error depends on not only some system parameters, such as the baseline B, wavelength λ, the look angle θ and the inclination of the baseline α, but also the rotation radius, location of the reflector, and the rotational angular velocity ω. The derived elevation errors vary with the change of azimuth positions, as shown in Fig. 6. The elevation error with different rotational angular velocities is also presented there. The maximum elevation error is related to the relative position of the strong scatterer and the InSAR antennas, while the minimum elevation error depends on the slow time t_a. With co-registration error due to low correlation considered, the DEM error will be larger than the current result.

Through our theoretical analysis, we can see that the circularly moving strong scatterers will produce

varying phase noise along the azimuth direction and reduce the correlation of two SLC images, both of which will increase the errors of the unwrapped phase. The unwrapped phase with the propagated phase errors has a direct impact on the precision of DEM. All these show that the circularly moving strong scatterer is a very promising jamming method in the field of InSAR electronic warfare.

IV. Simulation and Analysis

The aforementioned sections have analyzed the jamming effects on interferometric phase, correlation, and elevation estimation. In what follows, to demonstrate the performance of the proposed method, simulation results are provided based on the Terra-SAR system. The corner reflector, as a type of strong scatterer, is used in our simulation. The coverage and density of circularly moving strong scatterers are also discussed in detail.

A. Jamming Effects on Imaging and Interferometry

In this part, we analyze the jamming effects caused by the circularly moving corner reflector. Without loss of generality, a circularly moving corner reflector is placed at the center of the scene, as shown in Fig. 1(a) and (b). Assume that the size of the corner reflector is large enough to reach 35 dB of the input JSR [15]. To remove the effect of topography on interferometric processing, a flat terrain with an area of 1424 m×892 m (ground range and azimuth direction) is considered. Parameters of the circularly moving corner reflector are listed in Table I and those for the system and the scene are listed in Tables II and III, respectively. To acquire the final terrain elevation with jamming, the processing procedure of InSAR involves echo simulation [24], RD imaging [19], relevant registration [22], [25], interferometry [2], [3], phase filtering [26], phase unwrapping [26], [27] and elevation inversion [2], [4].

Since echo signals from the original scene and the corner reflector are received by the antennas

simultaneously, simulation of the SAR echo signals with interference is first performed. The two SLC images are produced through the Range-Doppler algorithm. Without loss of generality, only the master image is shown in Fig. 7(a). Clearly, the jamming output in the master image, shown as point series along azimuth, agrees with equation (15). Through co-registration and comparing both complex images, the interferometric phase with jamming is obtained and depicted in Fig. 7(b). The multiple discrete lines along the azimuth direction are caused by the point pairs. On the one hand, the phase noise is partly induced by phase errors, as shown in (30). On the other hand, the low correlation of the point pairs produces more phase noise, which is depicted in (26). As the interferometric phase is wrapped into the interval $[-\pi, \pi]$, it must be unwrapped before converting it to elevation result. After phase filtering, the unwrapped phase including the jamming effect is obtained by using the branch-cut phase unwrapping method [23], [24], as shown in Fig. 7(c). The jamming line is distributed along the azimuth direction. Furthermore, the failure of phase unwrapping can be observed in the right part of the figure.

Finally, DEM is produced according to the geometric relationship of the scene. To show the jamming effects more clearly, the DEM before and after jamming are respectively shown in Fig. 8(a) and (b). The DEM without jamming is displayed as a flat terrain, while the jammed one shows serious elevation errors. In Fig. 8(b), the elevation errors are composed of three parts. The first part, described in (32), is derived from phase errors due to the point series. The second part is due to the low correlation of the point pairs. Moreover, the failure of unwrapping can result in errors in the right part of the figure. It again demonstrates the effectiveness of the proposed jamming method.

B. Coverage Analysis

1) *In Azimuth:* The imaging output due to jamming is shown as point series or ghost points since the echoes spread over a number of azimuth cells. The expression (15) appears to show that the number of paired echoes is infinite in theory. However, $J_n\left[4\pi r_0(t_a)/\lambda\right]$ will approach to zero when n increases. The point series beyond the Doppler bandwidth will be folded over. According to Carson's rule [28], the number of the paired echoes is

$$N = \frac{8\pi}{\lambda} r_0(t_a) + 5 \approx \frac{8\pi}{\lambda} r \sin\theta + 5 \tag{33}$$

According to (15), the spacing Δx between those azimuth points can be derived as [20]

$$\Delta x = \left| \frac{\omega v}{2\pi K_{a1}} \right| = \frac{\omega \lambda R_M}{4\pi v} \tag{34}$$

Fig. 9 shows the influence of angular velocity on azimuth spacing, with corresponding parameters listed in Table I and Table II. Clearly, the spacing Δx will be larger as angular velocity increases. Then, the azimuth coverage of jamming can be obtained by combining (33) and (34)

$$L_a = \Delta x \cdot N = \left(2r \sin\theta + \frac{5\lambda}{4\pi} \right) \frac{\omega R_M}{v} \tag{35}$$

Equation (35) tells us that the azimuth coverage of the jamming depends on many parameters, including r, ω, λ, R_M, v, and θ. Larger radius r and angular velocity ω result in a larger azimuth jamming coverage, as shown in Fig. 10(a) and (b). In Fig. 10(c), the jamming coverage along azimuth doesn't vary over azimuth time for different radii and angular velocities. It proves the validity of the approximation in (33).

2) *In range:* According to (15), the range coverage of jamming is determined by the sinc function related to the fast time. Considering the RCM (Range Cell Migration) caused by the circularly moving corner reflector, (15) changes to

$$J_{m\_out}(t_r,t_a) \approx T_P T_L \cdot \mathrm{sinc}\left\{ B_r \left[t_r - \frac{2}{c}(R_M + \frac{r^2 + 2r\sqrt{{y_0}^2 + (vt_a - x_0)^2}\sin\left[\omega t_a + \theta_0 + \theta'_m(t_a)\right]}{2R_M}) \right] \right\}$$
$$\cdot \exp\left\{ -j\frac{4\pi}{\lambda}\left[R_M + \frac{r^2}{2R_M} \right] \right\} \sum_{n=-\infty}^{+\infty} J_n\left[\frac{4\pi}{\lambda} r_0(t_a) \right] \mathrm{sinc}\left\{ B_a\left(t_a - \frac{n\omega}{2\pi K_{a1}} - \frac{x_0}{v} \right) \right\} \exp\left\{ jn\left[\theta_0 + \theta'_m(t_a)\right] \right\} \tag{36}$$

Clearly, in (36), the jamming is spread over several range cells in the range direction and the range coverage of jamming can be approximated as

$$L_r \approx \rho_r + 2r\sin\theta \tag{37}$$

where ρ_r is range resolution of the InSAR system. So the range coverage of jamming is determined by ρ_r, r and θ. For typical parameters ($r = 1\mathrm{m}$, $\theta = 30°$, $\lambda = 0.03125\mathrm{m}$, $\omega = 15\pi\mathrm{rad/s}$, $R_M = 545.1\mathrm{km}$, $v = 7604\mathrm{m/s}$, $B_r = 130\mathrm{MHz}$), we have $L_a = 2.2660\mathrm{km}$ and $L_r = 2.1538\mathrm{m}$, i.e., a circularly moving corner reflector with a radius 1m and an angular velocity $15\pi\mathrm{rad/s}$ will create a jamming area of $2.2660\mathrm{km} \times 2.1538\mathrm{m}$, as shown in Fig. 7(a).

To increase the size of the jamming area, the circularly moving corner reflectors should be spaced with the azimuth grid of L_a and the range interval of L_r. So the size of such a jamming array will depend on the required jamming coverage and the size of the protected scenes. In designing such a system, we should also bear in mind that the jamming intensity is related to the backscattering coefficients of the corner reflector and the spacing Δx.

V. CONCLUSIONS

In this paper, an InSAR jamming method using circularly moving strong scatterers has been proposed. These scatterers are placed in the center of the scene and can cause serious errors in the

elevation measurement results of an InSAR system.

1) With the proposed jamming method, the imaging results will include paired echoes along the azimuth direction and the resultant phase interference of the paired echoes cannot be offset completely by comparing the two SLC images.

2) The proposed method will reduce the correlation of the two SLC images. After interferometry, the generated phase noise varies along the azimuth direction and can cause serious errors to the interferometric phase of the real scene.

3) Since the phase bias of the interference cannot be filtered out by the phase filter, it further increases the phase errors in the process of phase unwrapping and even leads to failure of the phase unwrapping operation.

4) The DEM produced with the proposed jamming method contains several errors: phase bias due to jamming, reduced correlation due to jamming and error propagation in phase unwrapping.

As also shown by our simulation results based on the Terra-SAR system, the proposed method can effectively jam the InSAR system and shows great promise in the field of electronic warfare. Furthermore, this jamming method also reveals a weak point of current InSAR systems, which provides a starting point for further improving the performance and robustness of InSAR systems in the future.

APPENDIX A

In this part, the effect of approximation on the accuracy of $r_0(t_a)$ is analyzed. According to (11), $r_0(t_a)$ can be rewritten as

$$r_0(t_a) = \frac{r\sqrt{y_0^2 + (vt_a - x_0)^2}}{R_M} = r\sqrt{\sin^2\theta + \left(\frac{vt_a - x_0}{R_M}\right)^2} \tag{A. 1}$$

Considering $vt_a - x_0 \ll R_M$, we have $r_0(t_a) \approx r\sin\theta$. The approximation error of $r_0(t_a)$ can be derived as

$$\Delta r_0(t_a) = r\sqrt{y_0^2 + (vt_a - x_0)^2}\left(\frac{1}{R_M} - \frac{1}{R_S}\right) \approx -\frac{rB\sin(\theta-\alpha)\sin\theta}{R_M} \tag{A. 2}$$

For $rB\sin(\theta-\alpha)\sin\theta \le rB \ll R_M$, the approximation error of $r_0(t_a)$ is very small and can be ignored. For typical parameters listed in Table II, the approximation error of $r_0(t_a)$ is shown in Fig. 11.

APPENDIX B

This appendix discusses the correlation of the jamming parts in the two SAR images. According to (15) and (16), the positions of ghost points are determined by sinc functions. In the azimuth direction, the position of corresponding point series in two SAR images depend on $n\omega/(2\pi K_{a1})$ and $n\omega/(2\pi K_{a2})$. Then, the time bias for the corresponding ghost points is given by

$$\Delta T_a = \frac{n\omega}{2\pi}\left(\frac{1}{K_{a1}} - \frac{1}{K_{a2}}\right) \tag{B.1}$$

where

$$K_{a1} = \frac{2v^2}{\lambda R_M}, \quad K_{a2} = \frac{2v^2}{\lambda R_S} \tag{B. 2}$$

Substituting (B. 1) into (B. 2), we have

$$\Delta T_a = \frac{n\omega\lambda}{4\pi v^2}\left(R_M - R_S\right) \approx \frac{n\omega\lambda B\sin(\theta-\alpha)}{4\pi v^2} \tag{B. 3}$$

The corresponding distance bias in the SAR image can be expressed as

$$X_{bias} = v\Delta T_a = \frac{n\omega\lambda B\sin(\theta-\alpha)}{4\pi v} \tag{B. 4}$$

Equation (B. 4) shows that the increasing ω will result in larger distance bias along azimuth. Using the parameters listed in Table II, the azimuth distance bias for the corresponding point series at different

angular velocities is calculated and shown in Fig. 12(a). Such distance bias will effectively reduce correlation of the jamming parts. In the range direction, the distance bias for the corresponding ghost points along range is determined by

$$Y_{bias} \approx 2r\sqrt{y_0^{\,2} + \left(vt_a - x_0\right)^2}\left\{\frac{\sin\left[\omega t_a + \theta_0 + \theta_m'(t_a)\right]}{R_M} - \frac{\sin\left[\omega t_a + \theta_0 + \theta_s'(t_a)\right]}{R_S}\right\} \qquad \text{(B. 5)}$$

Fig. 12(b) shows the range distance bias at $\omega = 15\pi$ rad/s. It will be larger with increase of the radius. Although the distance bias along range is small, considering the azimuth distance bias, the corresponding ghost points in two SAR images cannot be co-registered with each other. Therefore, we have $\gamma_J < \gamma_0$. Moreover, the low correlation of the jamming parts will reduce the correlation of original SAR images and generate more phase noise.

REFERENCES

[1] W. Chialin, K.Y. Liu, and M. Jin, "Modeling and a correlation algorithm for spaceborne SAR signals," IEEE Transactions on Aerospace and Electronic Systems, vol. AES-18, no. 5, pp. 563-575, Sep. 1982.

[2] A. Moccia and G. Rufino, "Spaceborne along-track SAR interferometry: performance analysis and mission scenarios," IEEE Transactions on Aerospace and Electronic Systems, vol. 37, no. pp. 199-213, Jan. 2001.

[3] G. Liao and H. Li, "Estimation method for InSAR interferometric phase based on generalized correlation steering vector," IEEE Transactions on Aerospace and Electronic Systems, vol. 46, no. 3, pp. 1389-1403, Jul. 2010.

[4] L. M. Zeger and R. K. Avent, “Terrain Effect Analysis for Cross-Track Stereo SAR Elevation Estimation,” IEEE Transactions on Aerospace and Electronic Systems, vol. 49, no. 4, pp. 2225-2234, Oct. 2013.

[5] L .Mingsheng, W. Teng, L. Lijun, Z. Wenjun, and L. Deren, “Reconstruction of DEMs from ERS-1/2 Tandem Data in mountainous area facilitated by SRTM,” IEEE Transactions on Geoscience and Remote Sensing, vol. 45, no. 7, pp. 2325-2335, Jul. 2007.

[6] W. Fan, W. Chao, Z. Hong, Z. Bo, and T. Yixian, “Rice Crop Monitoring in South China With RADARSAT-2 Quad-Polarization SAR Data,” IEEE Geoscience and Remote Sensing Letters, vol. 8, no.2, pp.196-200, Mar. 2011.

[7] N. Li, and Y. Zhang, “A survey of radar ECM and ECCM,” IEEE Transactions on Aerospace and Electronic Systems, vol. 31, no. 3, pp. 1110-1120, Jul. 1995.

[8] D. S. Garmatyuk, R. M. Narayanan, “ECCM capabilities of an ultrawideband bandlimited random noise imaging radar,” IEEE Transactions on Aerospace and Electronic Systems, vol. 38, no. 4, pp.1243-1255, Oct. 2002.

[9] M. Soumekh, “SAR-ECCM using phase-perturbed LFM chirp signals and DRFM repeat jammer penalization,” IEEE Transactions on Aerospace and Electronic Systems, vol. 42, no. 1, pp. 191-205, Jan. 2006.

[10] F. Zhou, B. Zhao, M. Tao, et al., “A Large Scene Deceptive Jamming Method for Space-Borne SAR,” IEEE Transactions on Geoscience and Remote Sensing, vol. 51, no. 8, pp. 4486-4495, 2013.

[11] W. P. Du Plessis, “Platform skin return and retrodirective cross-eye jamming,” IEEE Transactions on Aerospace and Electronic Systems, vol. 48, no. 1, pp. 490-501,2012.

[12] W. P. Du Plessis, J. W. Odendaal, J. Joubert, “Experimental simulation of retrodirective cross-eye jamming,” IEEE Transactions on Aerospace and Electronic Systems, vol. 47, no. 1, pp. 734-740, Jan. 2011.

[13] W. P. Du Plessis, J. W. Odendaal, J. Joubert, “Tolerance analysis of cross-eye jamming systems,” IEEE Transactions on Aerospace and Electronic Systems, vol. 47, no. 1, pp. 740-745, Jan. 2011.

[14] W. P. Du Plessis, “Limiting apparent target position in skin-return influenced cross-eye jamming,” IEEE Transactions on Aerospace and Electronic Systems, vol. 47, no. 3, pp. 2097-2101, 2013.

[15] Y. Xia, H. Kaufmann, X. Guo, “Differential SAR Interferometry Using Corner Refletors,” 2002 IEEE International Geoscience and Remote Sensing Symposium, vol. 2, pp. 1243-1246, Jun. 2002.

[16] Karabayir, Osman, et al, “Radar Cross Section and Doppler Effects of Wind Turbines on SAR Imaging,” Proceedings of 10th European Conference on Synthetic Aperture Radar, 2014.

[17] S. Chiu, P. Beaulne, “Ground Moving Target Indication Inside a Wind Farm: Interference and Mitigation,” Proceedings of 10th European Conference on Synthetic Aperture Radar, pp. 1-4, 2014.

[18] C. Clemente, J. J. Soraghan, “Analysis of the effect of wind turbines in SAR images,” IET International Conference on Radar Systems, 2012.

[19] Y. L. Neo, F. H. Wong, I. G. Cumming, “Processing of Azimuth-Invariant Bistatic SAR Data Using the Range Doppler Algorithm,” IEEE Transactions on Geoscience and Remote Sensing, vol. 46, no. 1, pp. 14-21, Jan. 2008.

[20] Li, Xiang, et al., “The influence of target micromotion on SAR and GMTI,” IEEE Transactions on Geoscience and Remote Sensing, vol. 49, no. 7, pp. 2738-2751, Jul. 2011.

[21] L. Kou, X. Wang, M. Xiang, et al. Interferometric estimation of three-dimensional surface deformation using geosynchronous circular SAR,” IEEE Transactions on Aerospace and Electronic Systems, vol. 48, vol. 2, pp. 1619-1635, Apr. 2012.

[22] H. A. Zebker and K. Chen, “Accurate estimation of correlation in InSAR observations,” IEEE Geoscience and Remote Sensing Letters, vol. 2, no. 2, pp. 124-127, Apr. 2005.

[23] H. Fattahi, and F. Amelung, “DEM Error Correction in InSAR Time Series,” IEEE Transactions on Geoscience and Remote Sensing, no. 99 pp. 1-11, Jan. 2013.

[24] H. Xu, J. Chen, B. Wang, and Y. Zhou, “Quick method of distributed small satellite synthetic aperture radar single-look complex image simulation,” Journal of Beijing University of Aeronautics and Astronautics, vol. 34, no. 4, pp. 445-449, Apr. 2006.

[25] F. Cuccoli, L. Facheris, and F. Sermi, “Coordinate registration method based on sea/land transitions identification for over-the-horizon sky-wave radar: Numerical Model and Basic Performance Requirements,” IEEE Transactions on Aerospace and Electronic Systems, vol. 47, vol. 4, pp. 2974-2985, Jun. 2011.

[26] J. J. Martinez-Espla ; T. Martinez-Marin, and J. M. Lopez-Sanchez, “A particle filter approach for InSAR phase filtering and unwrapping,” IEEE Transactions on Geoscience and Remote Sensing, vol. 47, no. 4, pp. 1197-1211, Apr. 2009.

[27] Y. Hanwen, L. Zhenfang, and B. Zheng, “A cluster-analysis-based efficient multibaseline phase-unwrapping algorithm,” IEEE Transactions on Geoscience and Remote Sensing, vol. 49, no. 1, pp. 478-487, Jan. 2011.

[28] X. F. Wu, “Study on motion modulation jamming techniques against SAR-GMTI,” Ph.D. dissertation, Nat. Univ. Defense Technol., Changsha, China, 2009.

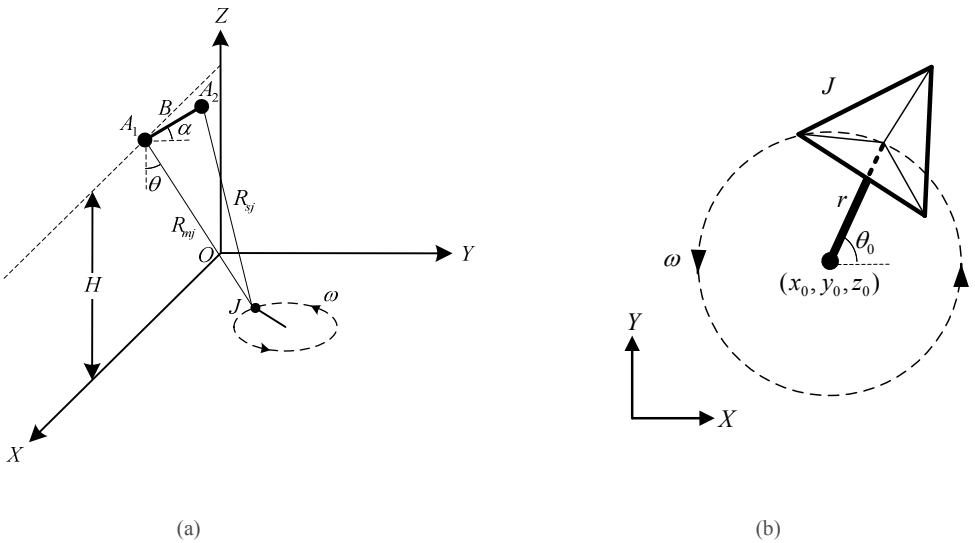

(a) (b)

Fig. 1. The jamming scenario. (a) InSAR and jammer geometry. (b) Circularly moving corner reflector on the horizontal plane.

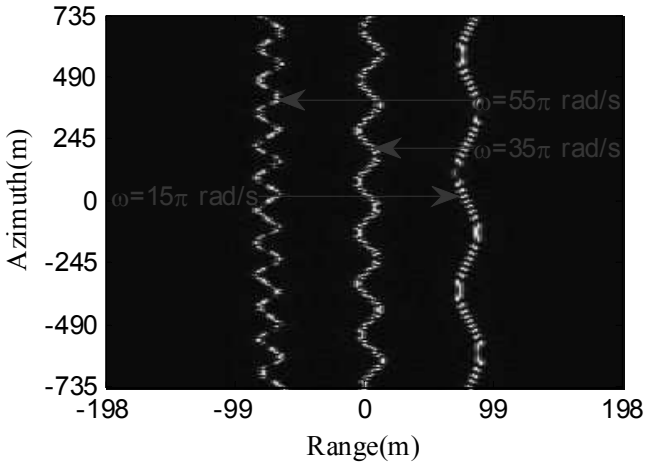

Fig. 2. Range compression result of jamming with r =8 m and $\omega = 55\pi$ rad/s, 35π rad/s, 15π rad/s.

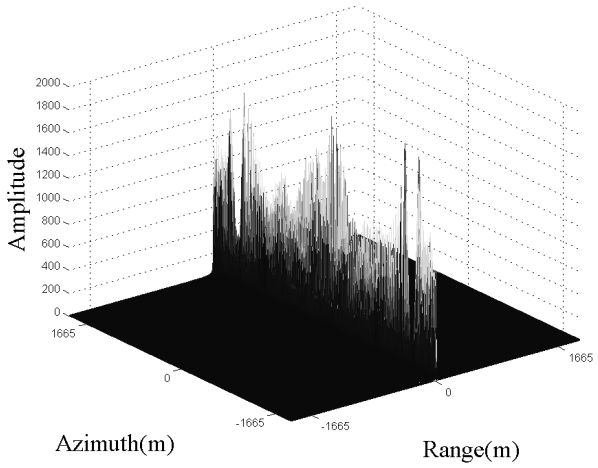

Fig. 3. Imaging result due to jamming.

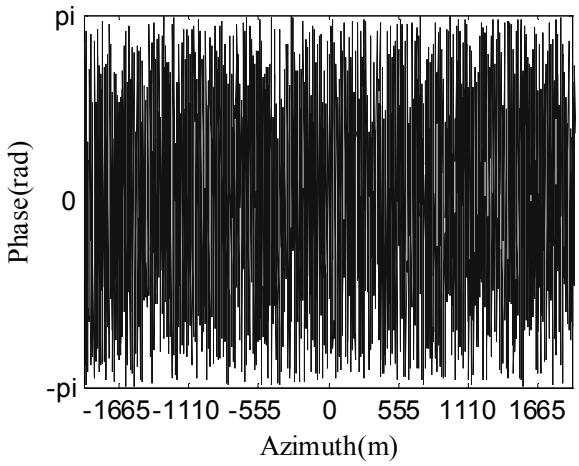

Fig. 4. Phase noise of the paired echoes after imaging.

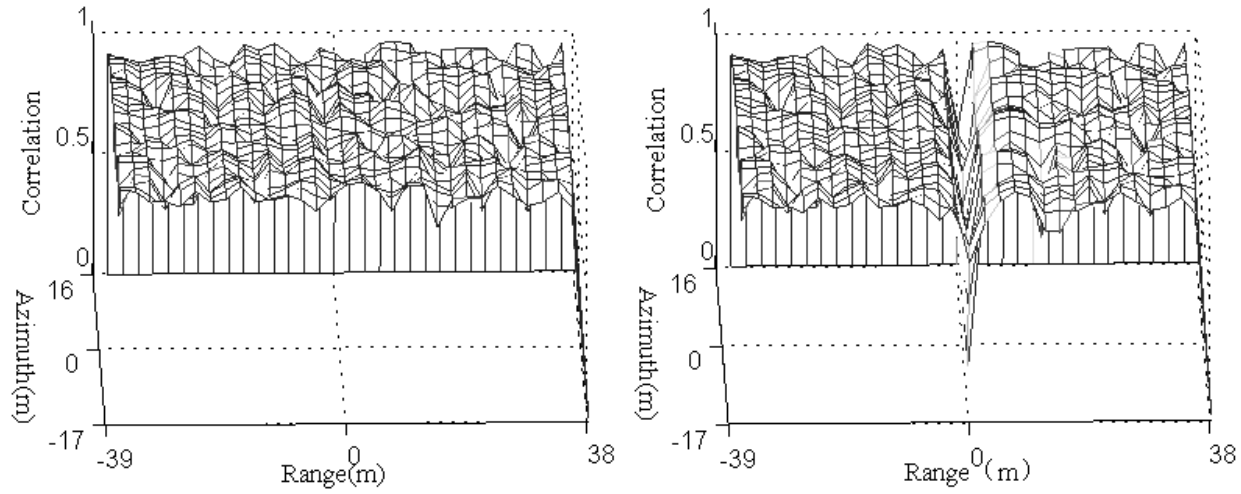

(a) (b)

Fig. 5. Comparison between correlation maps before and after jamming. (a) Correlation map before jamming. (b) Correlation map after jamming.

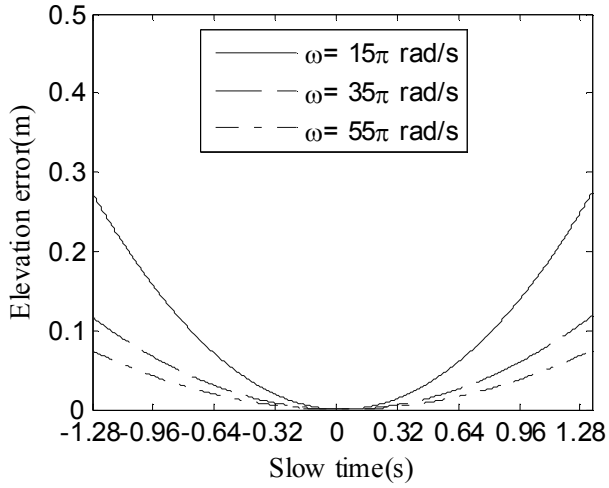

Fig. 6. Elevation error caused by circularly moving strong scatterer jamming.

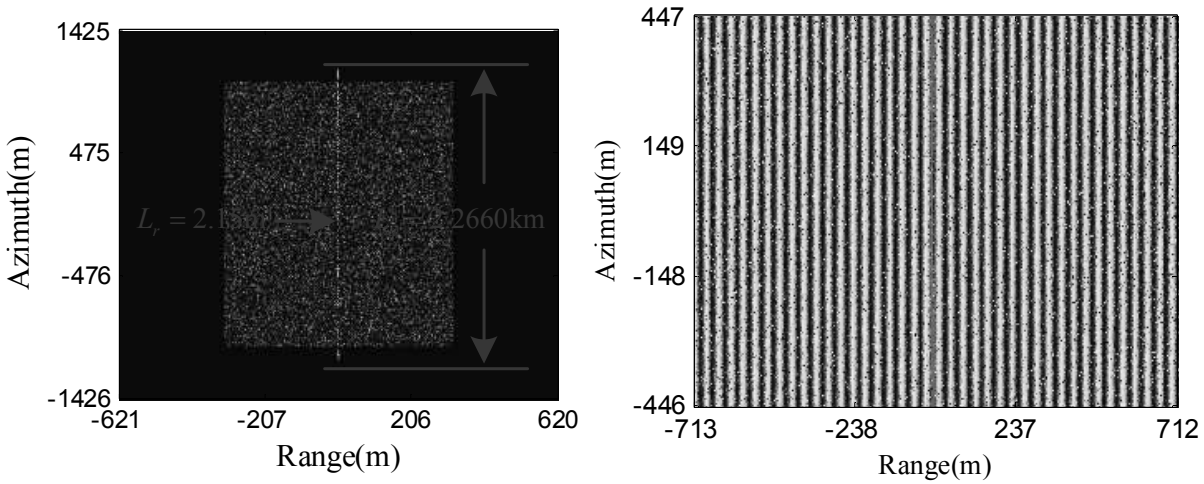

(a) (b)

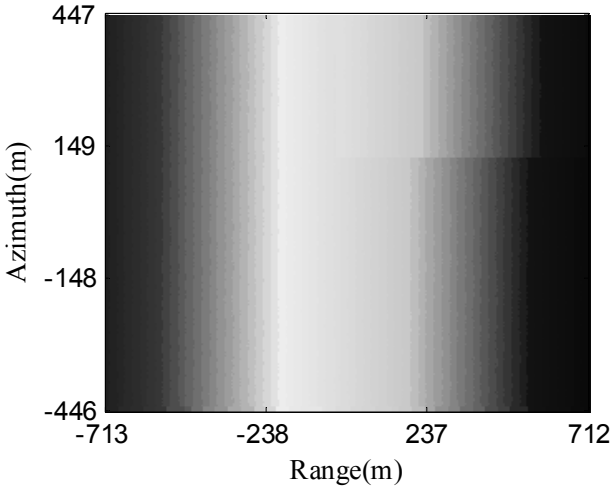

(c)

Fig. 7. Jamming effects on interferometry. (a) Master image with the jamming. (b) Interferometric phase. (c) Unwrapped phase.

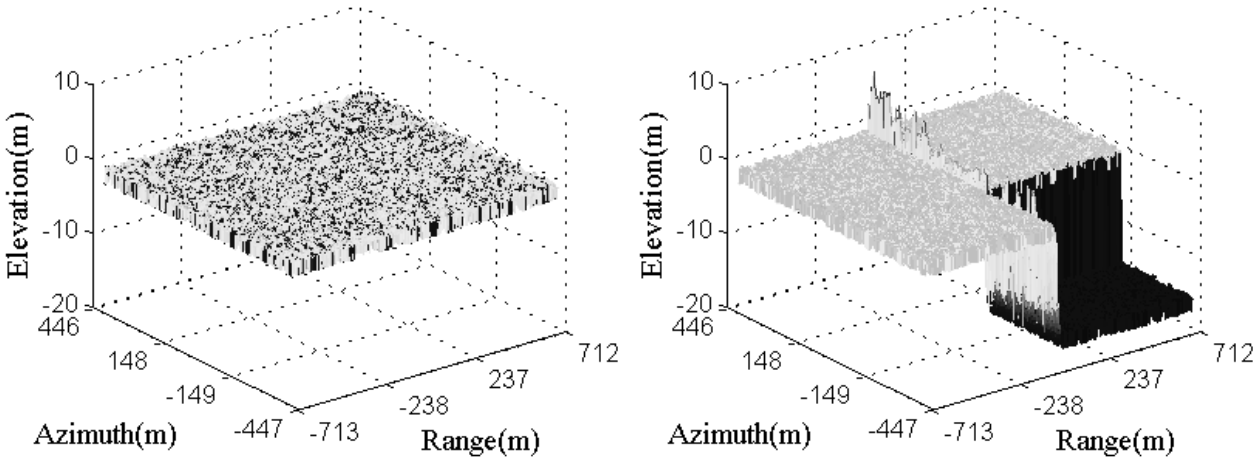

(a) (b)

Fig. 8. Comparison between DEMs before and after jamming. (a) DEM before jamming. (b) DEM after jamming.

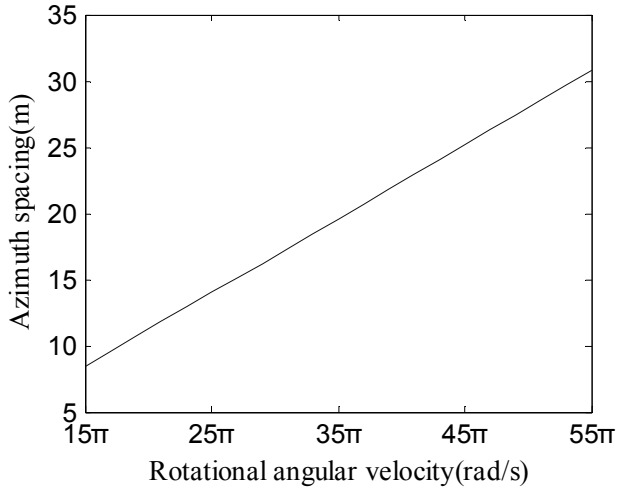

Fig. 9. The impact of rotational angular velocity on azimuth spacing of point series with $r = 1\text{m}$.

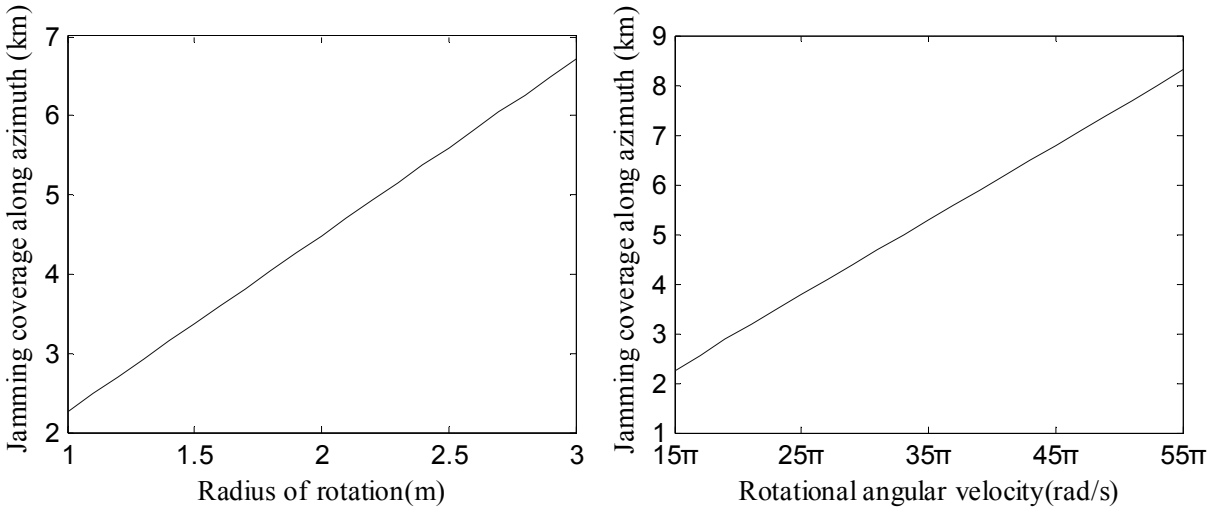

(a) (b)

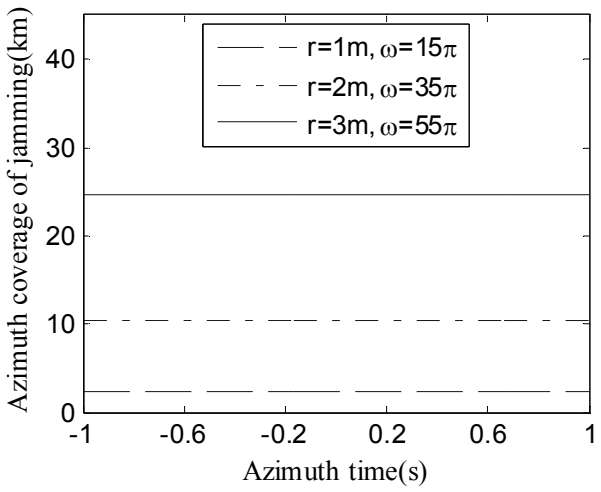

(c)

Fig.10. The impact of different parameters on jamming coverage along azimuth (using the parameters listed in Table II). (a) The impact of radius on the coverage at $\omega = 15\pi$. (b) The impact of angular velocity on the coverage with $r = 1\text{m}$. (c) The impact of azimuth time on the coverage.

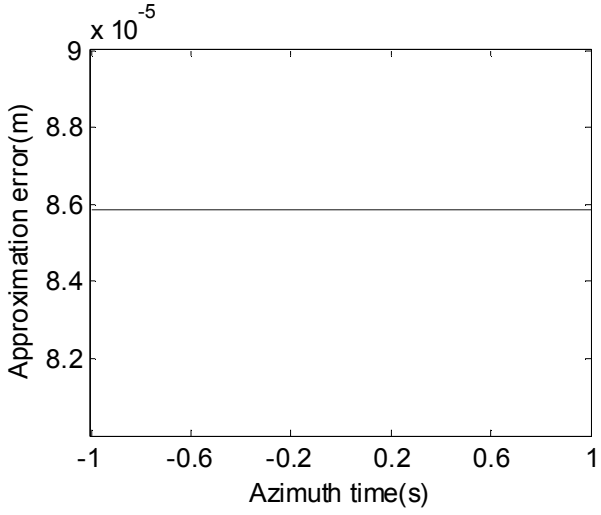

Fig. 11. The approximation error of $r_0(t_a)$.

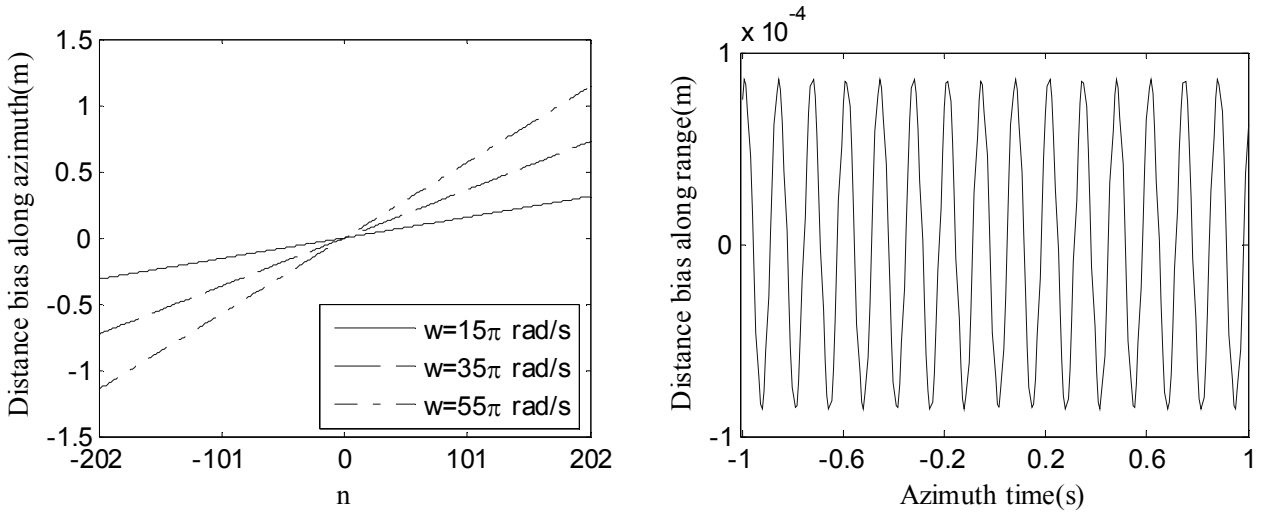

(a) (b)

Fig. 12. Distance biases for the corresponding point series. (a) The azimuth distance bias with different regular velocities. (b) The range distance bias at $\omega = 15\pi$ rad/s .

TABLE I

PARAMETERS OF THE CIRCULARLY MOVING CORNER REFLECTOR

Parameter	Value
Radius of gyration	1m
Angular velocity	15π rad/s
The initial angle value	0.3π rad

TABLE II

SIMULATION PARAMETERS OF THE INSAR SYSTEM

Parameter	Value
Carrier frequency	9.6GHz
Chirp rate	1.3×10^{13} Hz/s
Pulse duration	10μs
Sampling frequency	145MHz
Sensor velocity	7604m/s
Squint angle	0°
Center slant range	545.1km
Altitude	514.8km
Baseline length	200m
Baseline inclination	0°

TABLE III

SIMULATION PARAMETERS OF THE SCENE

Parameter	Value
Range point number	4096
Azimuth point number	4096
JSR	35dB